C. R. Mecanique 340 (2012) 602–618

Contents lists available at SciVerse ScienceDirect

Comptes Rendus Mecanique

www.sciencedirect.com

Pipe flow of shear-thinning fluids

Écoulement en conduite cylindrique de fluides rhéofluidifiants

Santiago Nicolas López-Carranza, Mathieu Jenny, Chérif Nouar *

LEMTA, université de Lorraine, CNRS UMR 7563, 2, avenue de la forêt de Haye, BP 160, 54504 Vandoeuvre lès Nancy, France

ARTICLE INFO

Article history:
Received 10 April 2012
Accepted after revision 9 May 2012
Available online 26 May 2012

Keywords:
Instability
Pipe flow
Non-Newtonian fluids
Spectral methods

Mots-clés :
Instabilité
Écoulement en conduite cylindrique
Fluides non-Newtoniens
Méthodes spectrales

ABSTRACT

Pipe flow of purely viscous shear-thinning fluids is studied using numerical simulations. The rheological behavior is described by the Carreau model. The flow field is decomposed as a base flow and a disturbance. The perturbation equations are then solved using a pseudo-spectral Petrov–Galerkin method. The time marching uses a fourth-order Adams–Bashforth scheme. In the case of an infinitesimal perturbation, a three-dimensional linear stability analysis is performed based on modal and non-modal approaches. It is shown that pipe flow of shear-thinning fluids is linearly stable and that for the range of rheological parameters considered, streamwise-independent vortices are optimally amplified. Nonlinear computations are done for finite amplitude two-dimensional disturbances, which consist of one pair of longitudinal rolls. The numerical results highlight a strong modification of the viscosity profile associated with the flow reorganization. For a given wall Reynolds number, shear-thinning reduces the energy gain of the perturbation. This is due to a reduction of the exchange energy between the base flow and the perturbation. Besides this, viscous dissipation decreases with increasing shear-thinning effects.

RÉSUMÉ

L'écoulement de fluides rhéofluidifiants en conduite cylindrique est étudié à l'aide de simulations numériques. Le comportement rhéofluidifiant est modélisé par la loi de Carreau. L'écoulement est décomposé en un écoulement de base et une perturbation. Les équations aux perturbations sont résolues en utilisant une méthode pseudo-spectrale de Petrov–Galerkin. La discrétisation temporelle utilise un schéma d'Adams–Bashforth d'ordre quatre. Dans le cas d'une perturbation infinitésimale, une analyse linéaire tridimensionnelle est effectuée suivant une approche modale puis non-modale. Les résultats obtenus montrent que dans la gamme des paramètres rhéologiques considérés, l'écoulement d'un fluide rhéofluidifiant est linéairement stable. La perturbation optimale est constituée d'une paire de rouleaux longitudinaux contra-rotatifs. Des simulations numériques non linéaires sont ensuite effectuées pour une perturbation bidimensionnelle d'amplitude finie constituée d'une paire de rouleaux longitudinaux. Les résultats numériques montrent que la réorganisation de l'écoulement s'accompagne d'une forte modification du profil de viscosité. En outre, pour une valeur donnée du nombre de Reynolds basé sur la viscosité pariétale, la rhéofluidification réduit l'amplification de l'énergie de la perturbation. On montre que cela est dû à la réduction des échanges d'énergie entre l'écoulement de base et

* Corresponding author.
E-mail address: cherif.nouar@univ-lorraine.fr (C. Nouar).

1631-0721/$ – see front matter
http://dx.doi.org/10.1016/j.crme.2012.05.002

la perturbation. Parallèlement à cela, la dissipation visqueuse décroit avec l'augmentation des effets rhéofluidifiants.

1. Introduction

Non-Newtonian fluids, such as colloidal suspensions, polymers or macro-molecules solutions are encountered in several industrial processes such as oil-well cementing, extrusion of molten polymers, paper coating, transport of mined slurries, etc. Many of these processes involve flows of non-Newtonian fluids through pipes. Knowledge of the flow structure is essential for an accurate design of pipe flow systems. In the laminar regime, the flow can be quite easily calculated. On the contrary, the transition to turbulence remains a genuine scientific challenge. Actually, this is also the case for Newtonian fluids, despite the numerous works done since Reynolds' experiment in 1883. The Hagen–Poiseuille flow is conjectured to be linearly stable for all Reynolds numbers and numerically proven [1] so for Reynolds number up to 10^7, yet it exhibits transition to turbulence at moderate flow velocities. A finite amplitude perturbation is therefore required to trigger transition to turbulence. In the last decade two different modeling approaches of transition to turbulence were proposed in the literature for Newtonian fluids. The first one is based on the algebraic transient growth exhibited by the optimal perturbations, which consist of streamwise counter-rotating vortices. These two-dimensional rolls evolve into streaks via the lift-up mechanism [2]. The resulting flow contains inflection points in the velocity profiles and can be unstable with respect to three-dimensional perturbations. This instability, which is typically studied by nonlinear direct simulations, is termed as streak breakdown. It was shown that this modeling approach is pertinent in parallel shear flows such as pipe Poiseuille flow [3], plane Poiseuille flow [4] and recently in magnetohydrodynamics channel flow [5]. The main goal of this approach is to determine the threshold amplitude of a perturbation required to trigger transition. The second approach seeks nonlinear wave solutions of the Navier–Stokes equations, by using the Self-Sustaining Process (SSP) initiated by Waleffe [6], and continuation methods. The SSP employs streamwise rolls, streaks and traveling waves as a fundamental building unit. Some unstable traveling waves solutions have been identified by Faisst and Eckhardt [7] and Wedin and Kerswell [8] for Newtonian pipe flow. Despite the fact that streaks, rolls and waves are all present in the exact coherent solution cited above, there is as yet no description of how such states might arise from the stable laminar base flow [9]. Recently, Biau and Bottaro [9] proposed an alternative optimization strategy, aimed at finding the optimal oblique waves yielding a self-sustained state. This optimization approach provides a proper match between the SSP theory and the optimal perturbation approach.

Comparatively to the Newtonian case, very few studies have been devoted to the transition to turbulence in a pipe for non-Newtonian fluids. This is perhaps not surprising, given the inherent additional complexities involved. There is a demand from industrial applications to predict the Reynolds number at which transition occurs. For instance, in the oil-well cementing process, turbulent flow is the preferred flow regime for efficient mud removal [10]. Therefore, a reliable criterion for the critical Reynolds number is needed to properly design the well-cleaning process with a minimum pump rate. Similarly, in the pipeline transport of slurries, in mining industry, turbulent flow is necessary to prevent particles from settling [11]. The existing literature reveals two interesting and yet unexplained effects. The first one concerns the delay in the transition to turbulence, more precisely in the onset of "puffs" [12–15]. For instance, Escudier et al. [14,15] investigated the transitional pipe flow of 0.15% w/w aqueous solution of xanthan gum (semi-rigid polymer) and 0.2% w/w polyacrylamide (flexible polymer). They found that the transition occurs at Reynolds number (defined with the bulk velocity, the pipe diameter and the wall shear-viscosity) about 3000 for xanthan gum and ≈ 4000 for polyacrylamyde. For a barite suspension (fluid used in oil-well cementing process) transition was found at Reynolds about 4000 [10]. The interpretation of the delayed transition is not straightforward, since the fluids considered, are both, to certain extent, shear-thinning (the viscosity decreases with increasing the shear-rate) and viscoelastic. Recently, Roland et al. [16] examined the effect of shear-thinning on the traveling waves found in Newtonian fluid. The authors focused only on the waves with an azimuthal wavenumber $n = 3$. They found that the critical Reynolds number of the saddle-node bifurcation where these waves appear increases when shear-thinning come into play. The second effect concerns the asymmetry of the mean axial velocity profiles observed in transitional regime [14,17,18,15,19], while in the laminar and turbulent regimes, the flow is axisymmetric. Here, "mean" refers to time-averaged. This asymmetry suggests the existence of a robust coherent structure characterized by two weakly modulated counter-rotating longitudinal vortices [18], i.e. with an azimuthal wavenumber $n = 1$. The asymmetry seems to be shear-thinning dependent. Indeed, non-Newtonian liquids with similar shear-thinning and different elastic behavior show the same degree of asymmetry [15].

The present work focuses on the pipe flow of purely viscous shear-thinning fluids, i.e., fluids without elasticity and for which the viscosity is a nonlinear function of the second invariant of the strain rate tensor. Additional nonlinear couplings between flow variables, in addition to the quadratic nonlinear inertial terms, appear in the momentum equations. Laminar flows of such fluids are mainly characterized by a stratification of the viscosity between the wall and the pipe axis: the viscosity decreases from the axis to the wall. To our knowledge the linear stability of the laminar flow of a shear-thinning fluid has not been performed before. Here it will be shown, for a wide range of the rheological parameters, that the flow is linearly stable, and that the optimal perturbation is constituted of streamwise-independent counter-rotating vortices. We will then study, with direct numerical simulation, the nonlinear development of the optimal perturbation, i.e. the first step

of the transition scenarios described above. More precisely, the objective is to examine the modification of the viscous dissipation induced by the viscosity perturbation, in presence of finite amplitude disturbance, and its consequence on the disturbance energy.

An outline of the article is as follows. The governing equations of the problem and the Carreau law as a model for shear-thinning behavior are given in dimensionless form in Section 2. The characteristics of the base flow in terms of velocity and viscosity profiles are discussed. The initial value problem for the perturbation field is stated. The presentation of the numerical method is made in Section 3. The dynamical system obtained is first solved in the case of an infinitesimal perturbation (linear theory) in Section 4. The validation of the numerical procedure and the convergence analysis for nonlinear computations are given in Section 5. The results for a finite perturbation are discussed in Section 6. Finally, conclusions on the main findings of the present work are drawn in Section 7.

2. Governing equations and base flows

2.1. Momentum equations – dimensionless parameters

We consider the flow of an incompressible purely viscous shear-thinning fluid in a circular pipe of radius $\hat{R}$. Here and in what follows, the quantities with a hat $(\hat{.})$ are dimensional. The governing equations in dimensionless form are

$$\nabla \cdot \boldsymbol{U} = 0 \tag{1}$$

$$\frac{\partial \boldsymbol{U}}{\partial t} + (\boldsymbol{U} \cdot \nabla)\boldsymbol{U} = -\nabla P + \nabla \cdot \boldsymbol{\tau} \tag{2}$$

where P is the pressure, including the gravity effect, and $\boldsymbol{\tau}$ the deviatoric stress tensor. The above equations have been rendered dimensionless using $\hat{W}_0$ the maximal velocity of the laminar flow as a velocity scale, the radius $\hat{R}$ of the pipe as a length scale, $\hat{R}/\hat{W}_0$ as a time scale and $\hat{\rho}\hat{W}_0^2$ as a stress and pressure scale. The velocity vector $\boldsymbol{U}$ is written as $\boldsymbol{U} = U\boldsymbol{e}_r + V\boldsymbol{e}_\theta + W\boldsymbol{e}_z$, where U, V and W are the velocity components in the radial, azimuthal and axial directions respectively. For purely viscous fluids, i.e. fluids for which the viscosity depends only on the shear rate, the deviatoric shear stress tensor

$$\boldsymbol{\tau} = \frac{1}{Re}\mu\dot{\boldsymbol{\gamma}} \quad \text{with } \dot{\boldsymbol{\gamma}} = \nabla\boldsymbol{U} + (\nabla\boldsymbol{U})^T \tag{3}$$

the strain-rate tensor. The Reynolds number

$$Re = \frac{\hat{\rho}\hat{W}_0\hat{R}}{\hat{\mu}_{ref}} \tag{4}$$

where the reference viscosity $\hat{\mu}_{ref}$ is defined afterwards. We focus on fluids of shear-thinning type. Many models are proposed in the literature to describe the dependence of viscosity on shear rate. Probably the most popular is the power-law model. However, this model gives an infinite viscosity as the shear rate tends to zero. A more realistic model is the Carreau–Yasuda model [20] for which the zero-shear rate viscosity $\hat{\mu}_0$ is finite. Using $\hat{\mu}_0$ as the reference viscosity, $\hat{\mu}_{ref} = \hat{\mu}_0$, the Carreau–Yasuda model in dimensionless form reads

$$\mu = \mu_\infty + (1-\mu_\infty)\left[1 + (\lambda\dot{\gamma})^a\right]^{(n_c-1)/a} \tag{5}$$

where $\mu_\infty = \hat{\mu}_\infty/\hat{\mu}_0$ is the dimensionless shear viscosity at infinite shear rate, $\lambda = \hat{\lambda}\hat{R}/\hat{W}_0$ is the dimensionless time constant of the fluid (its inverse is the dimensionless shear rate at which the onset of shear-thinning occurs), $n_c < 1$ is the shear-thinning index, a is a constant which describes the transition from the zero shear viscosity region to the power-law region. This five-parameter model offers the possibility to fit a wide variety of experimental data. However, for many polymer solutions, a good fit is obtained with $a = 2$, referred to as the Carreau model. One can note that the Newtonian fluid is recovered by setting any of the limits: $n_c = 1$, $\lambda = 0$ or $\mu_\infty = 1$. The dimensionless second invariant of the strain rate tensor $\dot{\gamma}$ is

$$\dot{\gamma} = \left[\frac{1}{2}\dot{\gamma}_{ij}\dot{\gamma}_{ij}\right]^{1/2} \tag{6}$$

2.2. Base flows

A one-dimensional shear flow, $\boldsymbol{U} = \boldsymbol{U}_b = W_b(r)\boldsymbol{e}_z$ is driven by a constant pressure gradient, i.e. the pressure $P_b = P_b^0 - G_p z$, with P_b^0 and G_p some constants. The subscript b means base flow. Then, the axial momentum equation reads

$$0 = G_p + \frac{1}{Re}\frac{1}{r}\frac{\mathrm{d}}{\mathrm{d}r}\left(r\mu_b\frac{\mathrm{d}W_b}{\mathrm{d}r}\right) \tag{7}$$

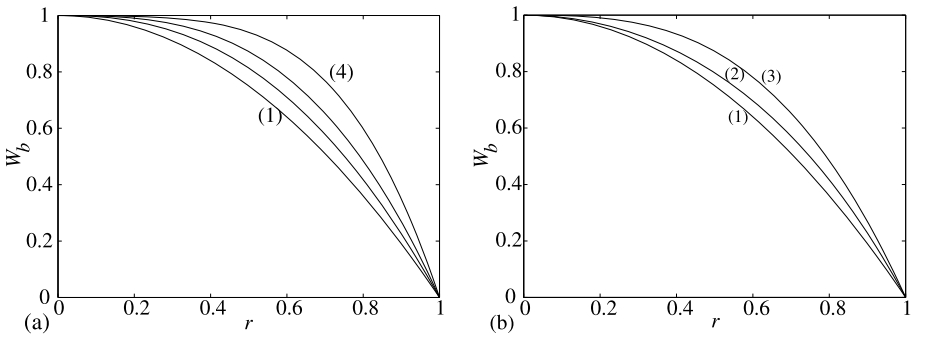

Fig. 1. Base velocity profiles. (a) $\lambda = 30$ and different values of the shear-thinning index: (1) $n_c = 1$ Newtonian fluid; (2) $n_c = 0.7$; (3) $n_c = 0.5$; (4) $n_c = 0.3$. (b) $n_c = 0.5$ and different values of the dimensionless time constant λ: (1) $\lambda = 0$ Newtonian fluid; (2) $\lambda = 1$; (3) $\lambda = 30$.

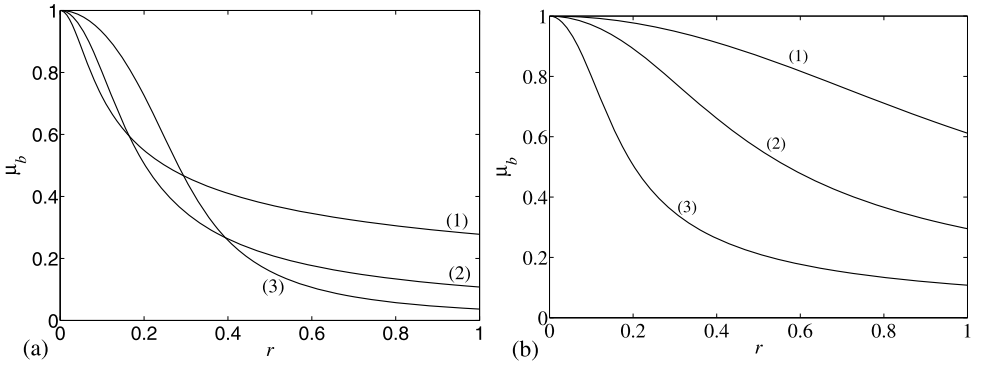

Fig. 2. Base viscosity profiles. (a) $\lambda = 30$ and different values of the shear-thinning index: (1) $n_c = 0.7$; (2) $n_c = 0.5$; (3) $n_c = 0.3$. (b) $n_c = 0.5$ and different values of the dimensionless time constant λ: (1) $\lambda = 1$; (2) $\lambda = 4$; (3) $\lambda = 30$.

where

$$\mu_b = \mu_\infty + (1 - \mu_\infty)\left(1 + \lambda^2\left(\frac{\mathrm{d}W_b}{\mathrm{d}r}\right)^2\right)^{(n_c-1)/2} \tag{8}$$

The above equations are supplemented by the no-slip condition at the wall. An iterative spectral method is used for solving the nonlinear equation (7). Since the center line velocity is the characteristic velocity, $W_b(0) = 1$. Hence, a specific pressure gradient has to be applied to produce $W_b(0) = 1$. Examples of the axial velocity profiles obtained at fixed λ and varying n_c, or fixed n_c and varying λ are given in Fig. 1. Hereafter, the infinite shear-rate viscosity is non-zero and is fixed, $\mu_\infty = 2 \times 10^{-3}$. This value is based on the rheological data given by Escudier et al. [15]. As expected, with increasing shear-thinning effects, the wall shear rate increases, and the velocity profile flattens in the central region. Fig. 2 shows the influence of shear-thinning effects with increasing λ or decreasing n_c on the viscosity profile. In order to highlight the viscosity sensitivity with respect to changes in the shear rate we define the quantity $vs = (1/\mu_b)(\mathrm{d}\mu_b/\mathrm{d}\dot{\gamma})$. As displayed in Fig. 3, vs increases with increasing shear-thinning effects. Furthermore, the curves of Fig. 3 highlight a strong sensitivity of the viscosity to change in $\dot{\gamma}$ near the axis, particularly for large values of λ (Fig. 3(b)).

2.3. Disturbance equations

The base flow is initially subjected to a disturbance $(\boldsymbol{u}, p)$: $\boldsymbol{U} = \boldsymbol{U}_b + \boldsymbol{u}$ and $P = P_b + p$. The equations governing the time-evolution of the disturbance are obtained by subtracting the base equations from (1), (2):

$$\nabla \cdot \boldsymbol{u} = 0 \tag{9}$$

$$\frac{\partial \boldsymbol{u}}{\partial t} = -(\boldsymbol{U}_b.\nabla)\boldsymbol{u} - (\boldsymbol{u}.\nabla)\boldsymbol{U}_b - (\boldsymbol{u}.\nabla)\boldsymbol{u} - \nabla p + \nabla.\left[\boldsymbol{\tau}(\mathbf{U}_b + \mathbf{u}) - \boldsymbol{\tau}(\mathbf{U}_b)\right] \tag{10}$$

with the no-slip boundary conditions on the pipe wall. In Eq. (10), the components of the deviatoric stress tensor of the disturbed flow are:

$$\tau_{ij}(\boldsymbol{U}_b + \boldsymbol{u}) = \frac{1}{Re}\mu(\boldsymbol{U}_b + \boldsymbol{u})\dot{\gamma}_{ij}(\boldsymbol{U}_b + \boldsymbol{u}) \tag{11}$$

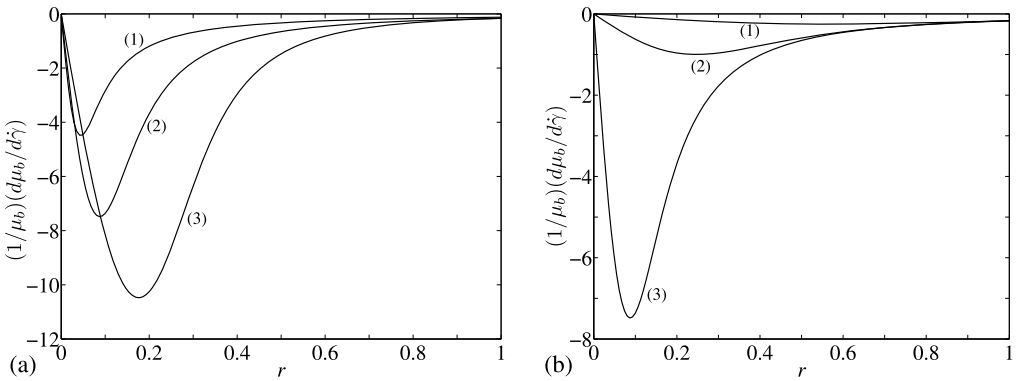

Fig. 3. Viscosity sensitivity. (a) $\lambda = 30$ and different values of the shear-thinning index: (1) $n_c = 0.7$; (2) $n_c = 0.5$; (3) $n_c = 0.3$. (b) $n_c = 0.5$ and different values of the dimensionless time constant λ: (1) $\lambda = 1$; (2) $\lambda = 4$ and (3) $\lambda = 30$.

As the fluid is supposed purely viscous, it was therefore assumed that the viscosity instantaneously adjusts the shear rate of the perturbed flow $\boldsymbol{U}_b + \boldsymbol{u}$. Physically, this assumes that the characteristic time of the reorganization of the internal structure is much smaller than the characteristic time of the perturbation.

3. Numerical method

Following Meseguer and Trefethen [21,1], a pseudo-spectral Petrov–Galerkin is used to integrate the governing equations. Fourier expansions are used in the azimuthal and axial directions, and Chebyshev-based functions are used in the radial direction. The expansion of the velocity, which is truncated at order L in z, order N in θ and order M in r, is written as:

$$\boldsymbol{u}_s(r,\theta,t) = \sum_{k=1,2}\sum_{l=-L}^{L}\sum_{n=-N}^{N}\sum_{m=0}^{M} a_{mnl}^{(k)}\boldsymbol{\Phi}_{mnl}^{(k)} \tag{12}$$

The trial bases $\boldsymbol{\Phi}_{mnl}^{(k)}$ are of the form:

$$\boldsymbol{\Phi}_{mnl}^{(k)} = \exp(iqz + in\theta)\boldsymbol{v}_{mnl}^{(k)}(r) \tag{13}$$

where $q = 2\pi l/Q$ is the axial wavenumber based on the axial periodicity Q of the flow, n the azimuthal wavenumber and $\boldsymbol{v}_{mnl}^{(k)}(r)$ a function based on the first kind Chebyshev polynomial $T_{2m}(r)$ [21]. The trial bases $\boldsymbol{v}_{mnl}^{(k)}(r)$ are given in Appendix A. The coefficients $a_{mnl}^{(k)}$ depend on time and satisfy the property $a_{mnl} = a_{m-n-l}^{*}$, since $\boldsymbol{u}_s$ is real. The star denotes the complex conjugate. By construction, the trial bases are divergence free, satisfy the no-slip condition at the wall and the regularity condition at the axis. Actually, the use of solenoidal basis functions of velocity appeared earlier in the literature [22]. Eq. (12) combined with (13) is substituted into Eq. (10) and a projection over solenoidal test fields $\boldsymbol{\psi}_{mnl}^{(k)}$, given in Appendix A which include the weight $1/\sqrt{1-r^2}$ and satisfying the boundary and the regularity conditions, is performed. The pressure term $-\nabla p$ cancels in the projection. The nonlinear inertial and viscous terms are calculated using a pseudo-spectral method. To avoid aliasing error, i.e., the production of small scales, the 3/2 padding rule for de-aliasing [23] is employed. Setting $\boldsymbol{a}$ the column vector containing the elements $a_{mnl}^{(k)}$, the dynamical system resulting from the projection procedure can be written as:

$$A\dot{\boldsymbol{a}} = B\boldsymbol{a} + \boldsymbol{b} \tag{14}$$

where $\boldsymbol{b}$, the column vector containing the nonlinear terms $b_{mnl}^{(k)}$, and the matrices A and B are defined such as:

$$[A\dot{\boldsymbol{a}}]_{mnl}^{(k)} = \langle \partial_t \boldsymbol{u}_s, \boldsymbol{\psi}_{mnl}^{(k)} \rangle \tag{15}$$

$$[B\boldsymbol{a}]_{mnl}^{(k)} = -\langle (\boldsymbol{U}_b \cdot \nabla)\boldsymbol{u}_s + (\boldsymbol{u}_s \cdot \nabla)\boldsymbol{U}_b, \boldsymbol{\psi}_{mnl}^{(k)} \rangle \tag{16}$$

$$b_{mnl}^{(k)} = -\langle (\boldsymbol{u}_s \cdot \nabla)\boldsymbol{u}_s, \boldsymbol{\psi}_{mnl}^{(k)} \rangle + \langle \nabla \cdot \boldsymbol{\tau}(\boldsymbol{U}_b + \boldsymbol{u}_s) - \boldsymbol{\tau}(\boldsymbol{U}_b), \boldsymbol{\psi}_{mnl}^{(k)} \rangle \tag{17}$$

The scalar product $\langle .,. \rangle$ is defined by the integration over the fluid domain of the functions product:

$$\langle \boldsymbol{\Phi}, \boldsymbol{\psi} \rangle = \int_0^{2\pi/q}\int_0^{2\pi}\int_0^{1} \boldsymbol{\Phi} \cdot \boldsymbol{\psi} r \, \mathrm{d}r \, \mathrm{d}\theta \, \mathrm{d}z \tag{18}$$

where $\boldsymbol{\Phi}$ belongs to the physical or trial space and $\boldsymbol{\psi}$ is a solenoidal vector belonging to the test space. The time discretization uses a fourth-order semi-implicit Adams–Bashforth scheme. The nonlinear terms (17) are calculated explicitly, while the linear terms (16) are integrated implicitly. Since the nonlinear viscous terms are integrated explicitly, the maximum allowable time step Δt which ensures the numerical stability decreases when the number of azimuthal and radial modes increases.

4. Case of infinitesimal three-dimensional perturbation: linear stability analysis

When the disturbance is infinitesimal, the nonlinear advective terms are neglected and the quantity $\boldsymbol{\tau}(\boldsymbol{U}_b + \boldsymbol{u}) - \boldsymbol{\tau}(\boldsymbol{U}_b)$ is linearized around the base flow $(\boldsymbol{U}_b, P_b)$,

$$\boldsymbol{\tau}' = \boldsymbol{\tau}(\boldsymbol{U}_b + \boldsymbol{u}) - \boldsymbol{\tau}(\boldsymbol{U}_b) = \mu(\boldsymbol{U}_b)\dot{\boldsymbol{\gamma}}(\boldsymbol{u}) + \mu'\dot{\boldsymbol{\gamma}}(\boldsymbol{U}_b) \tag{19}$$

Using Taylor expansion at first order, the viscosity perturbation μ' is given by

$$\mu' = \left.\frac{\partial \mu}{\partial \dot{\gamma}_{ij}}\right|_b \dot{\gamma}_{ij}(\boldsymbol{u}) \tag{20}$$

Since $\boldsymbol{U}_b = W_b(r)\boldsymbol{e}_z$, one has

$$\tau'_{ij} = \mu(\boldsymbol{U}_b)\dot{\gamma}_{ij}(\boldsymbol{u}) \quad \text{if } ij \neq rz, zr \tag{21}$$

$$\tau'_{ij} = \mu_t(\boldsymbol{U}_b)\dot{\gamma}_{ij}(\boldsymbol{u}) \quad \text{if } ij = rz, zr \tag{22}$$

with the "tangent viscosity"

$$\mu_t(\boldsymbol{U}_b) = \mu(\boldsymbol{U}_b) + \frac{\partial \mu}{\partial \dot{\gamma}_{rz}}(\boldsymbol{U}_b)\dot{\gamma}_{rz}(\boldsymbol{U}_b) \tag{23}$$

Indeed, for one-dimensional shear flow, with velocity $W_b(r)$ in the z-direction, the tangent viscosity is defined as $\mu_t = \partial\tau_{rz}/\partial\dot{\gamma}_{rz}$. For shear-thinning fluids $\mu_t < \mu$. One can note that the fluctuation stress tensor $\boldsymbol{\tau}'$ is anisotropic, due to viscosity perturbation. The initial value problem that results can be written

$$A\dot{\boldsymbol{a}} = L\boldsymbol{a} \tag{24}$$

with

$$[A\dot{\boldsymbol{a}}]^{(k)}_{mnl} = \left\langle \partial_t \boldsymbol{u}_s, \boldsymbol{\psi}^{(k)}_{mnl} \right\rangle \tag{25}$$

$$[L\boldsymbol{a}]^{(k)}_{mnl} = -\left\langle (\boldsymbol{U}_b \cdot \nabla)\boldsymbol{u}_s + (\boldsymbol{u}_s \cdot \nabla)\boldsymbol{U}_b, \boldsymbol{\psi}^{(k)}_{mnl} \right\rangle + \left\langle \nabla \cdot \boldsymbol{\tau}', \boldsymbol{\psi}^{(k)}_{mnl} \right\rangle \tag{26}$$

4.1. Modal approach: long-time behavior

When the long time behavior is sought, the disturbance is assumed to behave exponentially as $\exp(\sigma t)$. The initial value problem (25)–(26) is transformed into a generalized eigenvalue problem, with σ as eigenvalue:

$$\sigma A\boldsymbol{a} = L\boldsymbol{a} \tag{27}$$

The numerical results show that for the range of rheological parameters considered here, $0 < \lambda < 30$ and $0.3 < n_c < 1$, the real part of σ remains negative for all the eigenmodes. It is therefore conjectured that the pipe flow of a shear-thinning fluid $(0, 0, W_b(r))$ is linearly stable. The asymptotic behavior of the least stable mode was determined for two different kinds of perturbations $n = 1$, $q = 0$ and $n = 1$, $q = 1$. The same scaling as for Newtonian fluid is found when the Reynolds number is defined with the wall shear-viscosity $\mu_w = \mu_b(r = 1)$:

$$Re_w = Re/\mu_w \tag{28}$$

Hence, for the streamwise mode $n = 1$, $q = 0$, the least stable mode eigenvalue σ behaves as Re_w^{-1} and for $n = 1$, $q = 1$, the real part of the eigenvalues of the wall mode and the center mode behave as $Re_w^{-1/3}$ and $Re_w^{-1/2}$.

In the following, the results will be presented in terms of Re_w. It is worth noting here that the experimentalists [14,18,15] use μ_w in the Reynolds number definition. From a practical point of view, the tangential wall shear-stress τ_{rz} is determined from the measurement of the pressure gradient. The wall viscosity is then calculated from τ_{rz} and the rheological law.

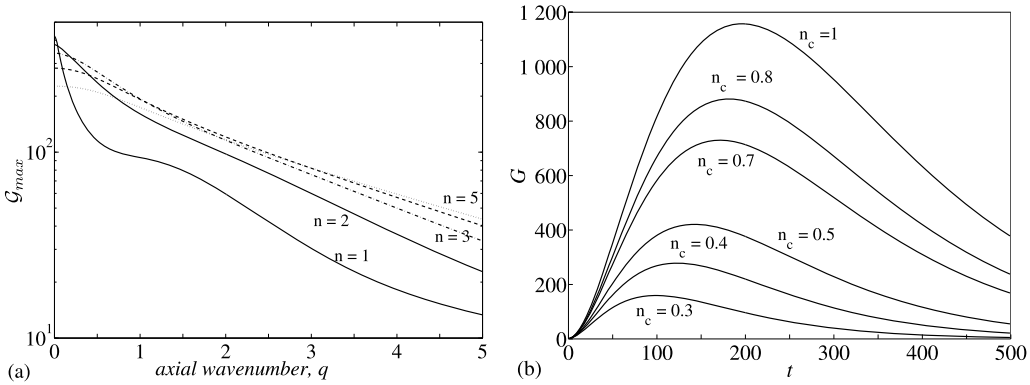

Fig. 4. (a) Maximum amplification of the disturbance kinetic energy as a function of the axial wavenumber q for different azimuthal wavenumbers n at $Re_w = 4000$, $\lambda = 30$ and $n_c = 0.5$. (b) Gain of kinetic energy for the optimal perturbation at $Re_w = 4000$, $\lambda = 30$ and different values of the shear-thinning index, n_c.

4.2. Non-modal approach: transient growth

As the linear operator $\mathbb{L} = A^{-1}L$ is non-normal, i.e. the eigenmodes are not orthogonal under the energy norm, transient growth of the kinetic energy of the perturbation is expected, before an exponential decay. To characterize the transient growth, we define the gain G of the kinetic energy at given time t and non-zero initial condition, $\boldsymbol{u}(t=0)$, as:

$$G\big(t, q, n, \boldsymbol{u}(t=0)\big) = \frac{E(t, \boldsymbol{u})}{E(t=0, \boldsymbol{u})} \tag{29}$$

where $E(t, \boldsymbol{u})$ is the instantaneous disturbance kinetic energy density, for a given mode, defined by

$$E(t, \boldsymbol{u}) = \frac{q}{4\pi^2} \int_0^{\frac{2\pi}{q}} \int_0^{2\pi} \int_0^{1} \boldsymbol{u}.\boldsymbol{u} r \, \mathrm{d}r \, \mathrm{d}\theta \, \mathrm{d}z \tag{30}$$

The maximum amplification of the kinetic energy over all non-zero initial conditions and over all times is

$$\mathcal{G}_{\max}(q, n) = \sup_{t>0} \mathcal{G}(t, q, n) \quad \text{with } \mathcal{G}(t, q, n) = \sup_{\boldsymbol{u}(t=0)\neq 0} G\big(t, q, n, \boldsymbol{u}(t=0)\big) \tag{31}$$

The optimal amplification over all the azimuthal and axial wavenumbers is defined by

$$\mathcal{G}^{opt} = \sup_{q,n} \mathcal{G}_{\max}(q, n) \tag{32}$$

The procedure to compute the optimal initial condition is outlined in [24]. For all the range of rheological and dynamical parameters considered here, it is found that the optimal transient growth is reached for a streamwise homogeneous perturbation ($q = 0$), with an azimuthal wavenumber $n = 1$ as in the case of a Newtonian fluid. Nonetheless, from a very low axial wavenumber, the maximum amplification of the kinetic energy of the perturbation is reached for higher azimuthal modes as indicated by Fig. 4(a) at $n_c = 0.5$, $\lambda = 30$ and $Re_w = 4000$. The amplification of the kinetic energy at $Re_w = 4000$, $n = 1$, $l = 0$, $\lambda = 30$ and different values of the shear-thinning index is displayed in Fig. 4(b). As can be observed, shear-thinning reduces significantly the amplification of the kinetic energy as well as the corresponding time where the maximum amplification is reached. These results may be anticipated on the basis of those obtained in [25]. Numerical results show for instance at $\lambda = 30$ that $\mathcal{G}^{opt}_{n_c\neq 1} \propto n_c^{1.66} \times \mathcal{G}^{opt}_{n_c=1}$ and $t^{opt}_{n_c\neq 1} \propto n_c^{0.67} \times t^{opt}_{n_c=1}$. For given n_c and λ, the dependence of $\mathcal{G}^{opt}$ and t^{opt} on Re_w has been studied. It is found that $\mathcal{G}^{opt}$ increases with Re_w. The scaling with Re_w^2 is recovered. Similarly the scaling of t^{opt} with Re_w is satisfied. The structure of the initial perturbation which ensures the optimal amplification of the kinetic energy is represented in Fig. 5. It consists of two counter-rotating streamwise vortices along the wall-normal direction. At $t = 0$, almost all the energy is in the azimuthal and radial components and only a negligible part is contained in the streamwise component. For instance for $n_c = 0.5$ and $\lambda = 30$, 67.87% of the energy is in the azimuthal component and 32.06% in the radial component of the velocity. These vortices allow the transfer of energy to the streamwise velocity components by the lift-up mechanism creating low and high speed streaks, displayed in Fig. 5(b). The location of maximum streamwise velocity approaches the wall with increasing shear-thinning effects.

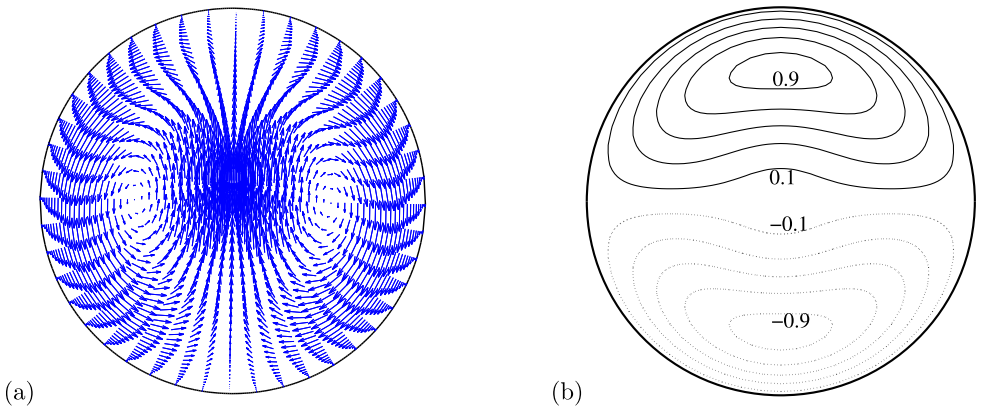

Fig. 5. (a) Optimal pattern of perturbation at $t = 0$ in the (r, θ) section, for $n_c = 0.5$, $\lambda = 30$ and $Re_w = 4000$. The arrows represent the vectors $u\boldsymbol{e_r} + v\boldsymbol{e}_\theta$. (b) Optimal streaks at $t = t^{opt} = 150$ time units: Iso-values of the axial velocity component w. Continuous lines for positives values of w: 0.1 near the wall with a step of 0.2 until 0.9. Dashed lines for negative values of w: -0.1 near the wall then with a step of -0.2 until -0.9.

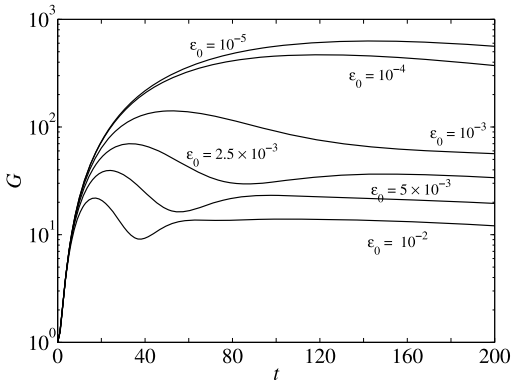

Fig. 6. Case of a Newtonian fluid. Energy amplification factor $G(t)$ of a two-dimensional streamwise perturbation at $Re = 3000$ and for different values of the initial energy ϵ_0. The results are obtained using $M = 6$ radial modes, $N = 9$ azimuthal modes and $\Delta t = 0.01$.

5. Nonlinear two-dimensional computations: validation and convergence

5.1. Validation

Firstly, Zikanov's result [3] corresponding to the energy amplification of two-dimensional perturbation, in the case of a Newtonian fluid, is reproduced in order to validate the computational code. The initial perturbation is in the form of a pair of streamwise rolls with azimuthal wavenumber $n = 1$. The normalized energy of an arbitrary perturbation $\boldsymbol{u}$ is defined by

$$\epsilon(\boldsymbol{u}) = \frac{E(t, \boldsymbol{u})}{E(\boldsymbol{U}_b)} \tag{33}$$

where $E(\boldsymbol{U}_b) = 1/6$ in the case of a Newtonian fluid. Fig. 6 shows the variation of the energy amplification $G(t)$. The results are in very good agreement with those given by Zikanov [3] and Meseguer [26]. It is interesting to note that the numerical computations started with the simplified expressions of the coefficients $a_{mn}^{(k)}$ proposed by Zikanov [3] and used by Meseguer [26] are not distinguishable from those obtained with the optimal perturbation, within plotting accuracy.

5.2. Convergence

5.2.1. Spatial convergence

In order to test the spatial convergence of the solution, computations are performed for different truncation levels (M_i, N_i). The relative variation of G with respect to the highest level of truncation (M_h, N_h) is defined by

$$\Delta G(t)_{M_i,N_i} = \frac{|G_{M_i,N_i} - G_{M_h,N_h}|}{G_{M_h,N_h}} \tag{34}$$

The truncation error is estimated by the maximum of $\Delta G(t)$ over all the time interval considered, typically $0 \leqslant t \leqslant 1000$. For instance, for an initial disturbance consisting of one pair of longitudinal rolls, at $n_c = 0.5$, $\lambda = 30$ and $Re_w = 4000$,

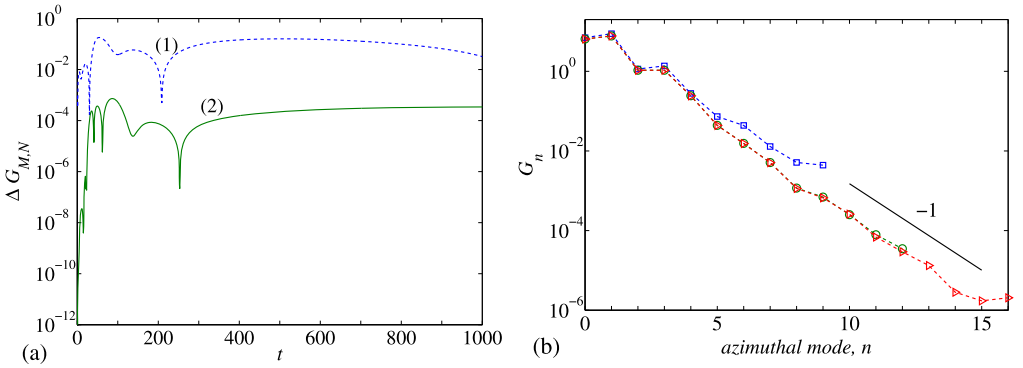

Fig. 7. Convergence test for a Carreau fluid $n_c = 0.5$, $\lambda = 30$ at $Re_w = 4000$. The initial perturbation is in the form of streamwise rolls with an energy $\epsilon_0 = 10^{-2}$. (a) Truncation error for two different spatial resolutions: (1) $(M_1 = 6, N_1 = 9)$ and (2) $(M_2 = 12, N_2 = 12)$, with $(M_h = 12, N_h = 16)$. (b) Energy spectra over the azimuthal modes at $t \approx 70$ and for the three truncation levels tested: (□) $(M = 6, N = 9)$; (○) $(M = 12, N = 12)$ and (▷) $(M = 12, N = 16)$.

computations were done for $(M, N) = (6, 9)$, $(12, 12)$ and $(12, 16)$. Fig. 7(a) displays ΔG vs time. For truncation levels $(M, N) = (6, 9)$ the error truncation is 18% obtained at $t = 54$ while it is 0.07% obtained at $t = 87$ for $(M, N) = (12, 12)$. There is no significant gain in accuracy of the solution, if one considers truncation level $(M \geqslant 12, N \geqslant 12)$. At an intermediate time $t \approx 70$, where ΔG is maximum, the spectral convergence of the solution is checked. This is illustrated by Fig. 7(b) where the energy distribution G_n over the azimuthal wavenumber n is displayed for the above three truncation levels. The ratio G_n of the kinetic energy associated to an azimuthal mode n, to that of the initial perturbation is

$$G_n = \frac{1}{E(t=0,\boldsymbol{u})} \sum_{k=1,2} \sum_{i=0}^{M} \sum_{j=0}^{M} \left[a_{in0}^{(k)*} a_{jn0}^{(k)} \int_0^1 \left(\boldsymbol{v}_{in0}^{(k)*}(r) . \boldsymbol{v}_{jn0}^{(k)}(r) r \, \mathrm{d}r \right) \right] \tag{35}$$

Fig. 7(b) shows that the spectral convergence is ensured when $M \geqslant 12$ and $N \geqslant 12$, with $G_n \propto \exp(-n)$. The test of spatial convergence described above is done for all the set of rheological and dynamical parameters studied.

5.2.2. Temporal convergence

The sensitivity of the computational results to the magnitude of the time step is examined by comparing the solutions $G(t)$ obtained with two time steps Δt and $\Delta t/2$. The convergence criterion is based on the maximum of the relative variation $|G(t)_{\Delta t} - G(t)_{\Delta t/2}|/G(t)_{\Delta t/2}$ which has to be less than 0.5%. Hence, for one pair of longitudinal rolls, at $n_c = 0.5$, $\lambda = 30$, $Re_w = 4000$, with $(M = 12, N = 12)$, the criterion of temporal convergence is ensured with $\Delta t = 10^{-2}$.

6. Nonlinear two-dimensional computations: results and discussion

The results section consists of four parts. Section 6.1 focuses on shear-thinning effects on the temporal evolution of the disturbance energy. Section 6.2 describes the flow structure and modification of the viscosity profiles. Section 6.3 gives the Reynolds–Orr equation and highlights the additional terms arising from the viscosity perturbation. Section 6.4 analyzes shear-thinning effects on each term of the energy equation. In the following, the dimensionless time constant in the Carreau model is fixed at $\lambda = 30$. This value is chosen in order to highlight clearly the shear-thinning effects. In addition, the results seem to be weakly dependent on λ when $\lambda \geqslant 20$.

6.1. Time evolution of the disturbance energy

The time evolution of the amplification factor $G(t)$ for a Carreau fluid with $n_c = 0.5$ is shown in Fig. 8(a). The initial energy $E_0 = E(t = 0, \boldsymbol{u})$ varies between 10^{-5} and 10^{-2} relative to the energy of the base flow. For a low value of $\epsilon_0 = E_0/E(\boldsymbol{U}_b)$, of the order of 10^{-5}, the contribution of the nonlinear terms can be neglected and we recover the transient growth due to the non-normality of the linear operator. For $\epsilon_0 > 2.5 \times 10^{-3}$, two stages can be distinguished in the evolution of the finite amplitude perturbation. In the first stage, at small t, the nonlinear curve follows the linear curve. The growth of the energy is mainly due to a "pseudo-linear" growth [3]. It is found that the maximum growth time is of order $\epsilon_0^{-1/2}$. The second stage is the nonlinear development of the perturbation. According to Waleffe [27], nonlinear inertial terms triggered by transients reduce the non-normality by adjusting the mean flow. This leads to a reduction of energy amplification factor G with increasing ϵ_0. Because of the z-independence of the perturbation, the rolls do not have an energy source and the flow undergoes, for $t \to +\infty$, a viscous decay back to the laminar regime. Qualitatively, the evolution $G(t)$ is similar to that of a Newtonian fluid. However, it is worth noting that for a given Re_w the amplification factor decreases with increasing shear-thinning effects as illustrated in Fig. 8(b). This reduction of G is more significant when the viscosity perturbation, μ', is not taken into account as illustrated in Fig. 9(a), where the amplification factor is reported as a function of time and

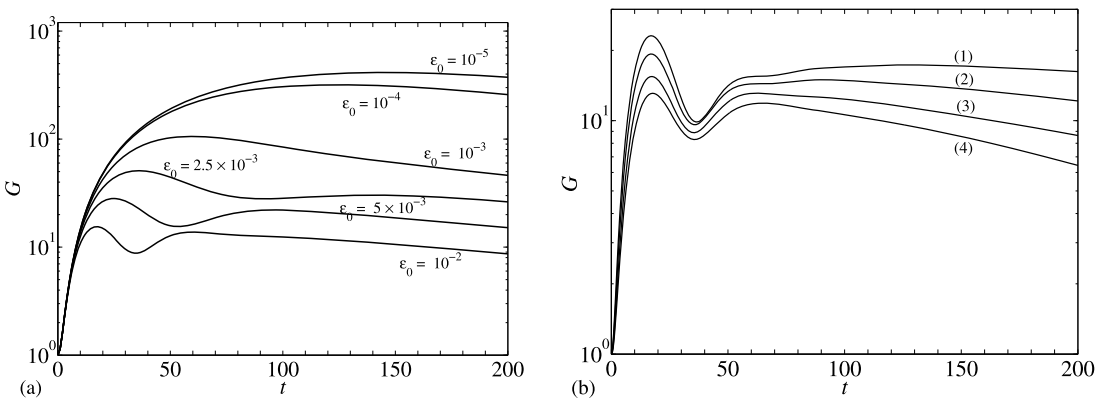

Fig. 8. (a) Energy amplification factor $G(t)$ of a two-dimensional streamwise perturbation for a Carreau fluid with $n_c = 0.5$ at $Re_w = 4000$ and different values of the initial energy ϵ_0. The curve obtained from linear transient growth is not distinguishable from that corresponding to $\epsilon_0 = 10^{-5}$. (b) Shear-thinning effects on the amplification factor G for $\epsilon_0 = 10^{-2}$: (1) $n_c = 1$ Newtonian case; (2) $n_c = 0.7$; (3) $n_c = 0.5$ and (4) $n_c = 0.4$.

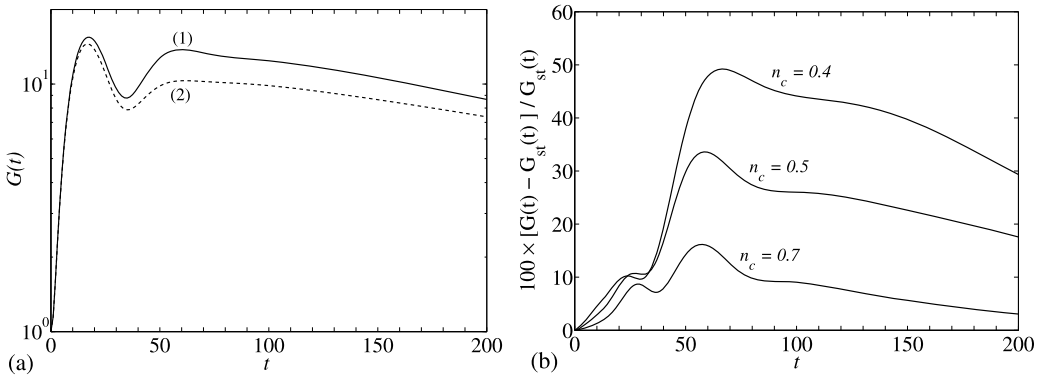

Fig. 9. (a) Energy amplification factor $G(t)$ of a two-dimensional streamwise perturbation for a Carreau fluid with $n_c = 0.5$ at $Re_w = 4000$: (1) the viscosity perturbation is taken into account, (2) the viscosity perturbation is not taken into account. (b) Relative variation between $G(t)$ calculated when the viscosity perturbation is taken into account and that calculated without taking into account the viscosity perturbation. This later case is called 'purely stratified case' and is indicated by the subscript *st*.

compared with the situation where μ' is artificially forced to zero. The relative variation of $G(t)$ between the two situations, where the viscosity perturbation is taken and not taken into account increases with increasing shear-thinning effects as it is shown in Fig. 9(b). These different results can be discussed in terms of the balance equation for the averaged disturbance kinetic energy equation. This analysis is deferred to a later section, after having described the time evolution of the flow structure and the modification of the viscosity profiles.

6.2. Flow structure and viscosity profiles

In order to emphasize the nonlinear effects, the amplitude of the initial disturbance has to be sufficiently important. The results given in this section are obtained for $\epsilon_0 = 10^{-2}$. In Fig. 10, we have represented the kinetic energy associated with each component u, v and w of the perturbation velocity. The radial and azimuthal kinetic energy decrease strongly, while the axial kinetic energy becomes rapidly dominant. Indeed, the counter-rotating vortices drag slow moving fluid into faster moving fluid, and lift faster moving fluid into slower moving fluid. This mechanism gives rise to the appearance of inflection points in the azimuthal profile of the streamwise velocity. This is clearly illustrated by Figs. 11(a)–11(c), where we have represented contours of constant streamwise velocity at three different times: $t = 5$ (first stage in $G(t)$), $t = 15$ (maximum growth time) and $t = 150$ (second stage in $G(t)$). They are analogous to that of Newtonian fluids. Nevertheless, for shear-thinning fluids, the contours are squeezed at the top of the cross-section where the viscosity is lower. The distortion of the axial velocity profile with respect to the base flow is shown in Fig. 12, for two azimuthal positions $\theta = 0$ and $\theta = \pi/2$. Here, θ is oriented counterclockwise, with $\theta = \pi/2$ the "vertical" axis of symmetry of the initial perturbation, see Fig. 5(a). As the fluid is advected downstream by a pressure-driven mechanism, the flow rate has a tendency to drop. This is a natural consequence of the energy transfer from the mean flow to disturbance. The distortion of the axial velocity profiles described above is accompanied by a significant modification of the shear-rate. The incidence on the viscosity profiles is shown in Fig. 13. At short time (Fig. 13(a)), a strong decrease of the viscosity is observed in the central zone of the pipe,

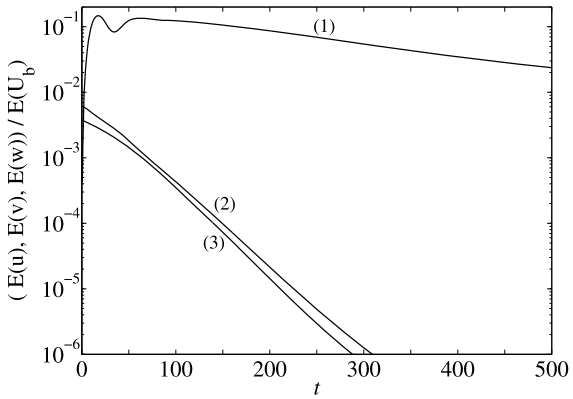

Fig. 10. Time evolution of the kinetic energy associated to: (1) axial $E(w)$, (2) azimuthal $E(v)$ and (3) radial $E(u)$, components of the velocity perturbation, at $n_c = 0.5$ and $Re_w = 4000$.

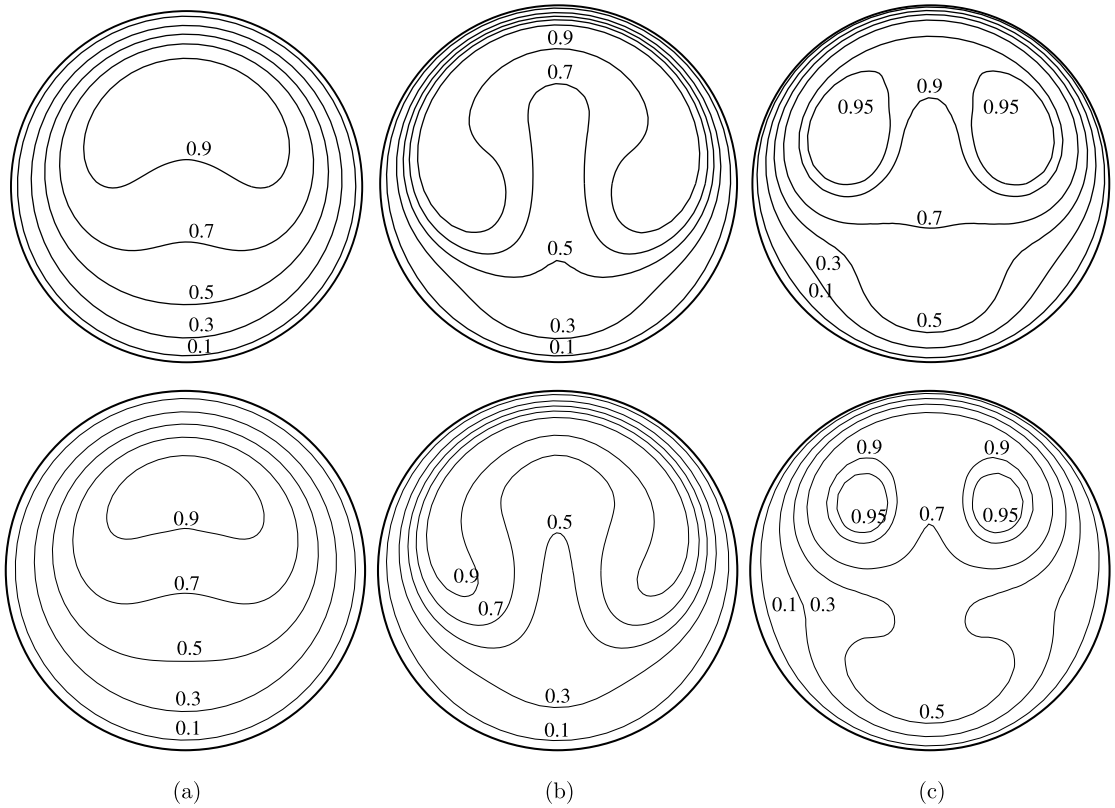

Fig. 11. Contours of constant streamwise velocity $W_b(r) + w(r, \theta, t)$ of the perturbed flow at $Re_w = 4000$ and $\epsilon_0 = 10^{-2}$. (a) $t = 5$; (b) $t = 15$ and (c) $t = 150$. (Top) Case of Carreau fluid with $n_c = 0.5$. (Bottom) Case of Newtonian fluid.

due to the high sensitivity of the viscosity to shear rate described in Fig. 3. Over time, the viscosity profile becomes more complex, but can still be analyzed from the corresponding axial velocity profile. It is clear that this strong modification of the viscosity profile affects the viscous dissipation.

6.3. Energy equation

It is useful to consider the Reynolds–Orr equation, to describe the time evolution of the kinetic energy of the disturbance. For this, we take the dot product of Eq. (10) with $\boldsymbol{u}$ and integrate over a cross-section. This yields

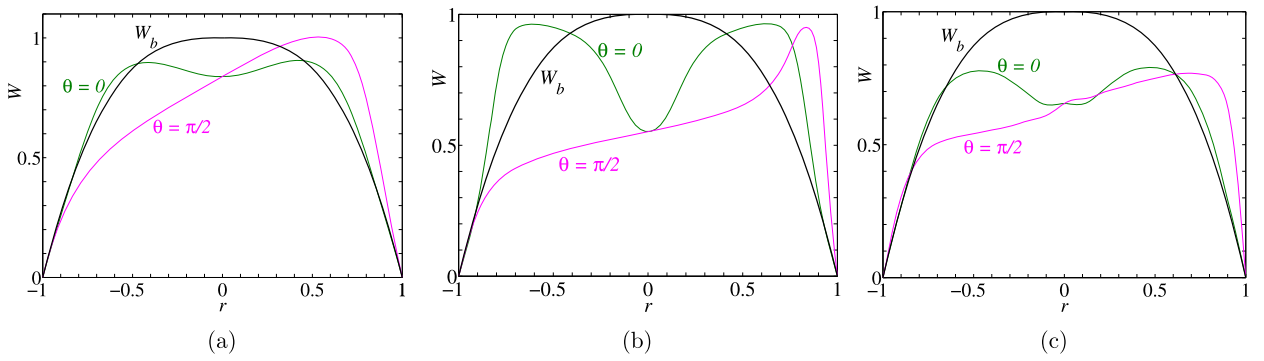

Fig. 12. Axial velocity profiles $W_b(r) + w(r,\theta,t)$ of the perturbed flow at two azimuthal positions (horizontal $\theta = 0$ and vertical $\theta = \pi/2$). Case of Carreau fluid with $n_c = 0.5$ at $Re_w = 4000$. The results are generated using $M = 12$ radial modes, $N = 12$ azimuthal modes and $\Delta t = 0.01$. (a) $t = 5$, (b) $t = 15$ and (c) $t = 150$.

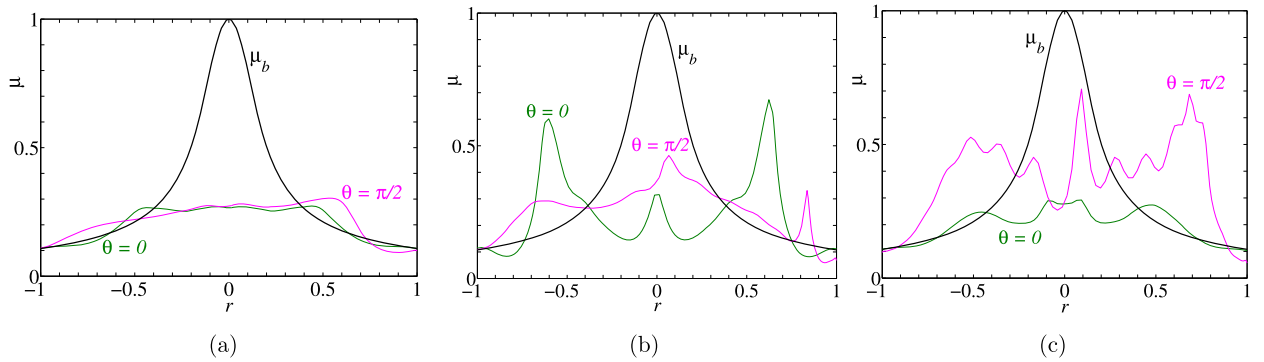

Fig. 13. Viscosity profiles $\mu(r,\theta,t)$. Case of Carreau fluid at $Re_w = 4000$ and $n_c = 0.5$. The results are generated using $M = 12$ radial modes, $N = 12$ azimuthal modes and $\Delta t = 0.01$. (a) $t = 5$, (b) $t = 15$ and (c) $t = 150$.

$$\frac{\mathrm{d}E}{\mathrm{d}t} = -\int_0^1\int_0^{2\pi} uw\frac{\mathrm{d}W_b}{\mathrm{d}r}r\,\mathrm{d}r\,\mathrm{d}\theta - \int_0^1\int_0^{2\pi}\frac{1}{2}\big[\tau_{ij}(\boldsymbol{U}_b+\boldsymbol{u}) - \tau_{ij}(\boldsymbol{U}_b)\big]\dot{\gamma}_{ij}(\boldsymbol{u})r\,\mathrm{d}r\,\mathrm{d}\theta \tag{36}$$

Eq. (36) can be written as

$$\frac{\mathrm{d}E}{\mathrm{d}t} = J + D \tag{37}$$

The first term J on the right-hand side of Eq. (37) is the rate of production of disturbance energy by the interaction of the Reynolds-stress uw and the mean velocity gradient $\mathrm{d}W_b/\mathrm{d}r$. The second term D is the rate of viscous dissipation. By introducing the viscosity perturbation $\mu' = \mu(\boldsymbol{U}_b + \boldsymbol{u}) - \mu(\boldsymbol{U}_b)$, the dissipation term can be written as the sum of three terms

$$D = D_1 + D_2 + D_3 \tag{38}$$

with

$$D_1 = -\frac{1}{Re}\int_0^1\int_0^{2\pi}\frac{1}{2}\mu_b\big(\dot{\boldsymbol{\gamma}}(\boldsymbol{u}):\dot{\boldsymbol{\gamma}}(\boldsymbol{u})\big)r\,\mathrm{d}r\,\mathrm{d}\theta$$

$$D_2 = -\frac{1}{Re}\int_0^1\int_0^{2\pi}\frac{1}{2}\mu'\big(\dot{\boldsymbol{\gamma}}(\boldsymbol{u}):\dot{\boldsymbol{\gamma}}(\boldsymbol{u})\big)r\,\mathrm{d}r\,\mathrm{d}\theta$$

$$D_3 = -\frac{1}{Re}\int_0^1\int_0^{2\pi}\mu'\dot{\gamma}_{rz}(\boldsymbol{u})\frac{\mathrm{d}W_b}{\mathrm{d}r}r\,\mathrm{d}r\,\mathrm{d}\theta \tag{39}$$

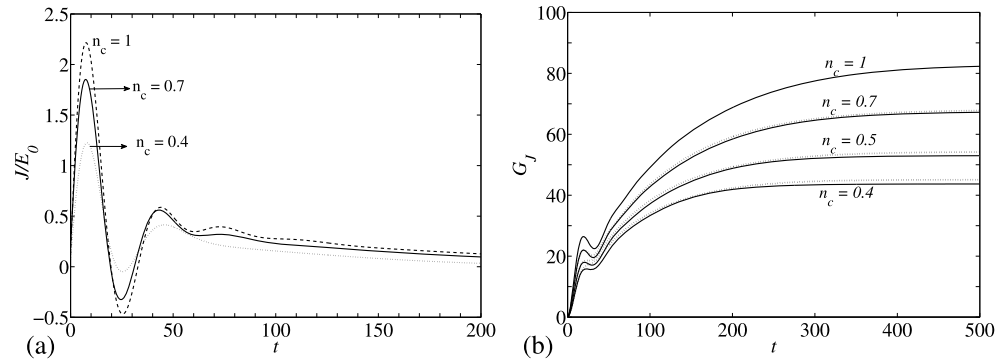

Fig. 14. Shear-thinning effects on the production of the disturbance energy by the interaction of the Reynolds stress with the base flow. (a) Time evolution of the production rate J/E_0. (b) Time evolution of $\langle J\rangle_t/E_0$: (dotted line) purely stratified case, (continuous line) the viscosity perturbation is taken into account.

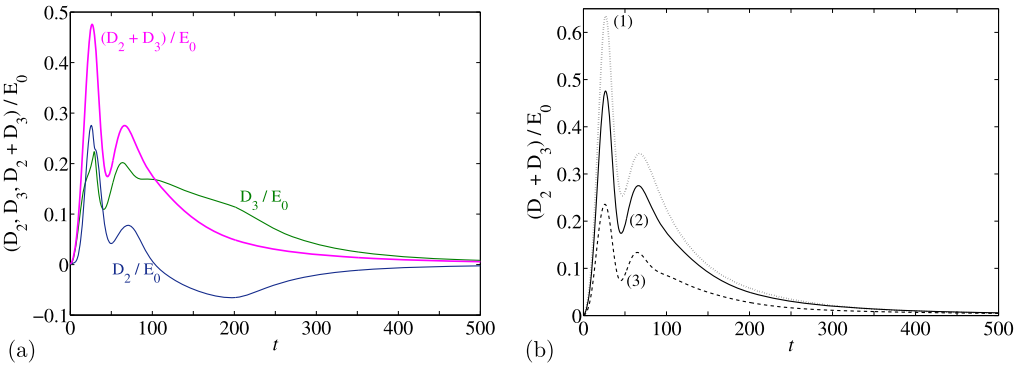

Fig. 15. (a) Time evolution of the additional terms D_2 and D_3 in the Reynolds–Orr equation arising from the viscosity perturbation at $n_c = 0.5$ and $Re_w = 4000$. (b) Effect of shear-thinning on $(D_2 + D_3)/E_0$: (1) $n_c = 0.4$, (2) $n_c = 0.5$ and (3) $n_c = 0.7$.

D_1 is the expression of the rate of viscous dissipation in the purely stratified case (μ' is artificially forced to zero). D_2 and D_3 are the modifications of the rate of viscous dissipation due to the viscosity perturbation. These two former terms vanish in the Newtonian case.

6.4. Analysis

6.4.1. Energy-exchange between the base flow and the disturbance

The production of disturbance kinetic energy by the interaction of the Reynolds stress with the base flow is examined in Fig. 14 for different values of the shear-thinning index. We have represented J/E_0 and $G_J = \langle J\rangle_t/E_0$, where $\langle(.)\rangle_t = \int_0^t (.)\,\mathrm{d}t$. The energy-exchange between the base-flow and the disturbance holds mainly in the "pseudo-linear" growth step. It decreases with increasing shear-thinning effects. One has to note that G_J evaluated in the purely stratified case (μ' forced to zero) is very close to that evaluated when the viscosity perturbation is taken into account (Fig. 14(b)).

6.4.2. Viscous dissipation terms

Fig. 15 shows the time evolution of the additional terms D_2 and D_3. The following observations can be made:

(i) At short time, D_2 is large and positive because of the strong decrease of the viscosity as explained previously.
(ii) As time increases, D_2 becomes negative and tends to zero.
(iii) D_3 is always positive. This term is the integral of the product of the "non-Newtonian Reynolds stress", $\mu'\dot{\gamma}_{rz}(\boldsymbol{u})$ with the mean velocity gradient. Actually, this product denoted d_3 is almost always positive. Using first-order Taylor approximation for μ' it can be shown straightforwardly that

$$d_3 = -\mu'\dot{\gamma}_{rz}(\boldsymbol{u})\,\mathrm{d}W_b/\mathrm{d}r \approx -\dot{\gamma}_{rz}^2(\boldsymbol{u})\left(\frac{\partial\mu}{\partial\dot{\gamma}_{rz}}\right)_b \frac{\mathrm{d}W_b}{\mathrm{d}r} \tag{40}$$

is positive for shear-thinning fluids. This is confirmed by the numerical computations. In Fig. 16, the distribution of d_3 is displayed in a (r,θ) section at different times. It is not surprising that, the maximal values of d_3 are attained mainly near the wall where the axial velocity gradient $\mathrm{d}W_b/\mathrm{d}r$ is larger.

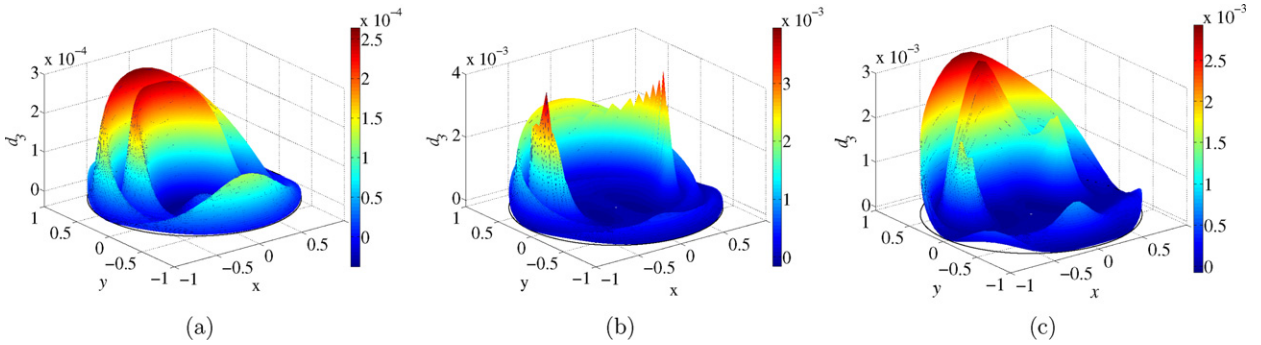

Fig. 16. Distribution in section r, θ of the non-Newtonian Reynolds stress at three different times: (a) $t = 5$; (b) $t = 15$ and (c) $t = 150$. The computation is done with $Re_w = 4000$ and $n_c = 0.5$.

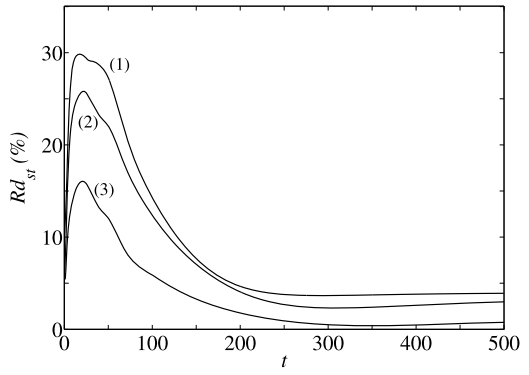

Fig. 17. Reduction of the viscous dissipation with respect to the purely stratified case: (1) $n_c = 0.4$; (2) $n_c = 0.5$ and (3) $n_c = 0.7$.

(iv) The sum of these two additional terms is positive. It increases with increasing shear-thinning effects. This can be related to the increase of the viscosity sensitivity to changes in the shear-rate as indicated by Fig. 3(a).

The importance of the additional terms D_2 and D_3 may be assessed by introducing the quantity Rd_{st} as:

$$Rd_{st} = \frac{\int_0^t [D_1(t') + D_2(t') + D_3(t') - D_{1st}(t')]\,\mathrm{d}t'}{-\int_0^t D_{1st}(t')\,\mathrm{d}t'} \tag{41}$$

which represents the reduction of the viscous dissipation with respect to the purely stratified case, where μ' is artificially canceled. Fig. 17 displays Rd_{st} as function of time for three different values of shear-thinning index. It is observed that Rd_{st} increases sharply, reaches a maximum within a short time then decreases asymptotically towards a constant value nearing zero. We note also that Rd_{st} increases with increasing shear-thinning effects, i.e., with increasing the viscosity sensitivity. This reduction of the viscous dissipation with respect to the purely stratified case can be viewed as an energy source term for the perturbation that explains the difference between curves (1) and (2) in Fig. 9(a). The contribution of the inertial term G_J is very close to that obtained for a purely stratified case, as it is shown in Fig. 14(b).

Finally, Fig. 18 displays the rate of viscous dissipation $D/E_0 = (D_1 + D_2 + D_3)/E_0$ as well as $G_D = \langle D/E_0 \rangle_t$ for different values of n_c. It is observed that shear-thinning reduces the viscous dissipation.

6.5. Discussion

Fig. 14(b) shows that the production of disturbance kinetic energy by the interaction of the Reynolds stress with the mean field, decreases with increasing shear-thinning effects. This mechanism is at the origin of the reduction of the amplification factor G indicated in Section 6.1. This result can be considered as an extension of that obtained by Govindarajan et al. [28] and Nouar et al. [25] when they studied the linear stability of the plane channel flow of a Carreau fluid. The authors [28,25] have shown that the stabilizing effect observed for shear-thinning fluids, is primarily due to reduced energy intake from the mean flow to the perturbation. Besides this, the total viscous dissipation given by $\int_0^t (D_1 + D_2 + D_3)\,\mathrm{d}t'$ decreases as n_c decreases.

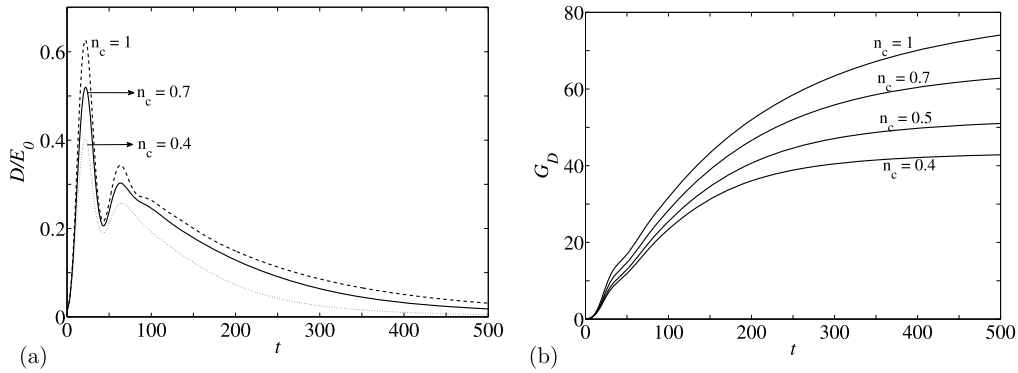

Fig. 18. Shear-thinning effects on the viscous dissipation. (a) D/E_0 versus time and (b) $\langle D/E_0\rangle_t$ versus time.

7. Conclusion

A pseudo-spectral Petrov–Galerkin computational code has been used to investigate the influence of the nonlinear dependence of the viscosity on the shear-rate, on the receptivity of pipe flow of shear-thinning fluids with respect to finite two-dimensional disturbances. The code has been validated for Newtonian fluids by comparison with Zikanov's [3] and Meseguer's [26] results. The linear stability analysis performed for a wide range of rheological parameters shows that pipe flow of shear-thinning fluids is linearly stable. The optimal perturbation is achieved for a two-dimensional perturbation with an azimuthal wavenumber $n = 1$ similar to the Newtonian case. It is then used as an initial condition for the nonlinear problem. For a sufficient initial energy ϵ_0, the longitudinal rolls give rise to streaks and inflection points. The viscosity profile is strongly modified by the perturbation. The consequence of this modification is analyzed through the Reynolds–Orr equation. Two additional terms arising from the viscosity perturbation appear which reduce significantly the viscous dissipation, with respect to the purely stratified case (case where $\mu' = 0$). Globally, the viscous dissipation decreases with increasing shear-thinning effects. The decrease of the amplification factor with increasing shear-thinning effects is ascribed to the reduced energy intake from the mean flow. These results indicate that shear-thinning effects contribute on one hand in the delay of transition observed experimentally [14,15] and on the other hand to the reduction in the friction coefficient [12].

A natural perspective to the present study is to analyze the influence of the shear-thinning effects on the stability of the 2D solutions obtained with respect to very small streamwise-dependent perturbation, i.e. the next step in the streak-breakdown scenario for transition to turbulence. This mechanism could be used to characterize the basin of attraction of Poiseuille flow of shear-thinning fluids.

Acknowledgement

The authors are very grateful to E. Plaut and J.P. Brancher for grateful discussions.

Appendix A. Trial and test fields

The choice of trial and test fields has been discussed in the papers [21,26,29]. For the purpose of completeness, we list these functions here. They are defined in terms of the functions:

$$h_m(r) = \left(1 - r^2\right) T_{2m-2}(r), \qquad g_m(r) = \left(1 - r^2\right) h_m(r) \tag{42}$$

with T_m the Chebyshev polynomial of degree m, and of the operators:

$$D = \frac{\mathrm{d}}{\mathrm{d}r}, \qquad D_+ = D + \frac{1}{r} \tag{43}$$

A.1. Trial fields

In the case $n = 0$,

$$\begin{aligned} \boldsymbol{v}_{m0l}^{(1)} &= r h_m \mathbf{e}_\theta \\ \boldsymbol{v}_{m0l}^{(2)} &= -ilr g_m \mathbf{e}_r + D_+(r g_m)\mathbf{e}_z \end{aligned} \tag{44}$$

except that, if $l = 0$,

$$\boldsymbol{v}_{m00}^{(2)} = h_m \mathbf{e}_z \tag{45}$$

In the case $n \neq 0$,

$$\boldsymbol{v}_{mnl}^{(1)} = -inr^{\sigma-1} g_m \mathbf{e}_r + D\big(r^{\sigma} g_m\big)\mathbf{e}_\theta$$
$$\boldsymbol{v}_{mnl}^{(2)} = -ilr^{\sigma+1} h_m \mathbf{e}_\theta + inr^{\sigma} h_m \mathbf{e}_z \tag{46}$$

with $\sigma = \sigma(n) = 1$ if n is odd, 2 if n is even.

A.2. Test fields

The test fields are of the form

$$\boldsymbol{\psi}_{mnl}^{(k)} = \exp[2\pi i lz/Q + in\theta]\tilde{\boldsymbol{v}}_{mnl}^{(k)}(r) \tag{47}$$

Let's introduce the Chebyshev weight function

$$\mathcal{W} = \frac{1}{\sqrt{1-r^2}} \tag{48}$$

The functions $\tilde{\boldsymbol{v}}_{mnl}^{(k)}(r)$ are: In the case $n = 0$,

$$\tilde{\boldsymbol{v}}_{m0l}^{(1)} = \mathcal{W} h_m \mathbf{e}_\theta$$
$$\tilde{\boldsymbol{v}}_{m0l}^{(2)} = \mathcal{W}\big\{-ilr^2 g_m \mathbf{e}_r + \big[D_+\big(r^2 g_m\big) + r^3 h_m\big]\mathbf{e}_z\big\} \tag{49}$$

except that, if $l = 0$,

$$\tilde{\boldsymbol{v}}_{m00}^{(2)} = \mathcal{W} r h_m \mathbf{e}_z \tag{50}$$

In the case $n \neq 0$,

$$\tilde{\boldsymbol{v}}_{mnl}^{(1)} = \mathcal{W}\big\{-inr^{\beta} g_m \mathbf{e}_r + \big[D\big(r^{\beta+1} g_m\big) + r^{\beta+2} h_m\big]\mathbf{e}_\theta\big\}$$
$$\tilde{\boldsymbol{v}}_{mnl}^{(2)} = \mathcal{W}\big(-ilr^{\beta+2} h_m \mathbf{e}_\theta + inr^{\beta+1} h_m \mathbf{e}_z\big) \tag{51}$$

except that, if $l = 0$,

$$\tilde{\boldsymbol{v}}_{mn0}^{(2)} = \mathcal{W} inr^{1-\beta} h_m \mathbf{e}_z \tag{52}$$

with, $\beta = \beta(n) = 1$ if n is odd, 0 if n is even.

References

[1] Á. Meseguer, L.N. Trefethen, Linearized pipe flow to Reynolds number 10^7, J. Comput. Phys. 186 (1) (2003) 178–197.
[2] M.T. Landahl, A note on an algebraic growth instability of inviscid parallel shear flows, J. Fluid Mech. 98 (2) (1980) 243–251.
[3] O.Y. Zikanov, On the instability of pipe Poiseuille flow, Phys. Fluids 8 (11) (1996) 2923–2932.
[4] S.C. Reddy, P.J. Schmid, J.S. Baggett, D.S. Henningson, On the stability of streamwise streaks and transition thresholds in plane channel flows, J. Fluid Mech. 365 (1998) 269–303.
[5] D. Krasnov, M. Rossi, O. Zikanov, T. Boeck, Optimal growth and transition to turbulence in channel flow with spanwise magnetic field, J. Fluid Mech. 596 (2008) 73–101.
[6] F. Waleffe, On a self-sustaining process in shear flows, Phys. Fluids 9 (4) (1997) 883–900.
[7] H. Faisst, B. Eckhardt, Travelling waves in pipe flow, Phys. Rev. Lett. 91 (22) (2003) 224502.
[8] H. Wedin, R.R. Kerswell, Exact coherent structures in pipe flow: Travelling wave solutions, J. Fluid Mech. 508 (2004) 333–371.
[9] D. Biau, A. Bottaro, An optimal path to transition in a duct, Proc. R. Soc. A 367 (2009) 529–544.
[10] F. Brand, J. Peixinho, C. Nouar, A quantitative investigation of the laminar-to-turbulent transition: Application to efficient mud cleaning, in: Proceedings of the SPE Annual Technical Conference and Exhibition, New Orleans, LA, United States, 2001.
[11] A.L. Mular, D.N. Halbe, D.J. Barrat, Mineral Processing Plant Design, Practice and Control, SME, vols. 1–2, 2002.
[12] M.P. Escudier, F. Presti, S. Smith, Drag reduction in the turbulent pipe flow of polymers, J. Non-Newtonian Fluid Mech. 81 (3) (1998) 197–213.
[13] A.A. Draad, G.D.C. Kuiken, F.T.M. Nieuwstadt, Laminar–turbulent transition in pipe flow for Newtonian and non-Newtonian fluids, J. Fluid Mech. 377 (1998) 267–312.
[14] M.P. Escudier, R.J. Poole, F. Presti, C. Dales, C. Nouar, C. Desaubry, L. Graham, L. Pullum, Observations of asymmetrical flow behaviour in transitional pipe flow of yield-stress and other shear-thinning liquids, J. Non-Newtonian Fluid Mech. 127 (2–3) (2005) 143–155.
[15] M.P. Escudier, S. Rosa, R.J. Poole, Asymmetry in transitional pipe flow of drag-reducing polymer solutions, J. Non-Newtonian Fluid Mech. 161 (1–3) (2009) 19–29.
[16] N. Roland, E. Plaut, C. Nouar, Petrov–Galerkin computation of nonlinear waves in pipe flow of shear-thinning fluids: First theoretical evidences for a delayed transition, Comput. Fluids 39 (2010) 1733–1743.
[17] J. Peixinho, C. Nouar, C. Desaubry, B. Théron, Laminar transitional and turbulent flow of yield stress fluid in a pipe, J. Non-Newtonian Fluid Mech. 128 (2–3) (2005) 172–184.
[18] A. Esmael, C. Nouar, Transitional flow of a yield-stress fluid in a pipe: Evidence of a robust coherent structure, Phys. Rev. E 77 (5) (2008) 057302.
[19] B. Guzel, T. Burghelea, I.A. Frigaard, D.M. Martinez, Observation of laminar–turbulent transition of a yield stress fluid in Hagen–Poiseuille flow, J. Fluid Mech. 627 (2009) 97–128.

[20] R.B. Bird, R.C. Armstrong, O. Hassager, Dynamics of Polymeric Liquids, vol. 1, Fluid Mechanics, Wiley Interscience, New York, 1987.
[21] Á. Meseguer, L.N. Trefethen, A spectral Petrov–Galerkin formulation for pipe flow (ii): Nonlinear transitional stages, Oxford University, Numerical Analysis Group, Rep. 01/19, 2001.
[22] A. Leonard, A. Wray, A new numerical method for the simulation of three-dimensional flow in a pipe, in: Proceedings of the 8th International Conference on Numerical Methods in Fluid Dynamics, Aachen, West Germany, 1982.
[23] C. Canuto, M. Hussaini, A. Quarteroni, T. Zang, Spectral Methods in Fluid Dynamics, Springer-Verlag, 1988.
[24] P.J. Schmid, D.S. Henningson, Stability and Transition in Shear Flows, Springer-Verlag, New York, 2001.
[25] C. Nouar, A. Bottaro, J.P. Brancher, Delaying transition to turbulence in channel flow: Revisiting the stability of shear-thinning fluids, J. Fluid Mech. 592 (2007) 177–194.
[26] Á. Meseguer, Streak breakdown instability in pipe Poiseuille flow, Phys. Fluids 15 (5) (2003) 1203–1213.
[27] F. Waleffe, Transition in shear flows. Nonlinear normality versus non-normal linearity, Phys. Fluids 7 (12) (1995) 3060–3066.
[28] R. Govindarajan, S. L'vov, I. Procaccia, A. Sameen, Stabilization of hydrodynamic flow by small viscosity variations, Phys. Rev. E 67 (2003) 026310, 11 pp.
[29] Á. Meseguer, F. Mellibovsky, On a solenoidal Fourier–Chebyshev spectral method for stability analysis of the Hagen–Poiseuille flow, Appl. Numer. Math. 57 (8) (2007) 920–938.